Interannual variability of the subsurface eddy field in the Southeast Pacific

Citation	Combes, V., Hormazabal, S., & Di Lorenzo, E. (2015). Interannual variability of the subsurface eddy field in the Southeast Pacific. Journal of Geophysical Research: Oceans, 120(7), 4907-4924. doi:10.1002/2014JC010265
DOI	10.1002/2014JC010265
Publisher	John Wiley & Sons Inc.
Version	Version of Record
Terms of Use	http://cdss.library.oregonstate.edu/sa-termsofuse

AGU PUBLICATIONS

JGR

Journal of Geophysical Research: Oceans

RESEARCH ARTICLE

10.1002/2014JC010265

Interannual variability of the subsurface eddy field in the Southeast Pacific

Vincent Combes[1], Samuel Hormazabal[2], and Emanuele Di Lorenzo[3]

[1]College of Earth, Ocean and Atmospheric Sciences, Oregon State University, Corvallis, Oregon, USA, [2]Escuela de Ciencias del Mar, Pontificia Universidad Catolica de Valparaiso, Valparaiso, Chile, [3]College of Earth and Atmospheric Sciences, Georgia Institute of Technology, Atlanta, Georgia, USA

Key Points:
- Model results indicate an asymmetry between surface and subsurface eddy fields
- The subsurface field is dominated by anticyclones
- The variability of the ITEs is significantly correlated with ENSO

Correspondence to:
V. Combes,
vcombes@coas.oregonstate.edu

Citation:
Combes, V., S. Hormazabal, and E. Di Lorenzo (2015), Interannual variability of the subsurface eddy field in the Southeast Pacific, *J. Geophys. Res. Oceans*, *120*, 4907–4924, doi:10.1002/2014JC010265.

Received 24 JUN 2014
Accepted 28 MAY 2015
Accepted article online 2 JUN 2015
Published online 16 JUL 2015

Abstract The Southeast Pacific, which encompasses the coasts of Peru and Chile, is one of the world's most productive regions resulting principally from the upwelling of subsurface nutrient-rich waters. Over the satellite altimetry era, there have been numerous evidence that surface mesoscale eddies play an important role in the offshore transport of rich coastal waters, but it has been only recently that few observational/numerical studies have highlighted the importance of the subsurface eddies. The eddy field variability is explored using the results of a high-resolution model experiment from 1979 to 2012. The model results indicate an asymmetry of the surface and subsurface eddy fields. While surface-intensified cyclones are slightly more frequent than anticyclones, the subsurface field is dominated by anticyclones (IntrathermoclineEddies; ITEs), triggered by the instability of the subsurface Peru Chile undercurrent (PCUC). Composite maps are consistent with in situ observations. ITEs are associated with maximum vorticity around 150–200 m depth, warmer and more saline core, characteristic of the equatorial subsurface water from the PCUC. We find that the variability of the ITEs is significantly correlated with the ENSO equatorial signal. During strong El Niño events (e.g., 1982; 1998), we find that while the PCUC transport increases, the volume of coastal waters transported by ITEs however decreases during those periods. We find that the relaxation of the isopycnals along the coast during El Niño events leads to weakened baroclinic instability and to a decrease of the ITEs transport.

1. Introduction

The South East Pacific (SEP), also referred to as the Humboldt Current System, is defined as the region that extends from 40°S to 5°S which encompasses the coasts of Chile and Peru. The deep ocean circulation in the SEP is characterized by the equatorward flow Peru-Chile Current, which is a branch of the Antarctic Circumpolar Current that advects cold subantarctic water along the coasts of Chile and Peru and into the South Equatorial Current. At the coast, the SEP is associated with high biological productivity and ecosystem efficiency driven by the upwelling of cold, nutrient-rich water brought to the surface. The coastal upwelling is, however, not spatially nor temporally uniform. It is persistent along the coasts of Peru, it weakens toward northern Chile and it varies seasonally in central Chile (similarly to the Oregon upwelling system) [*Strub et al.*, 1998]. The coastal oceanic circulation in the SEP shows strong interannual variations that are associated with a wide range of physical processes, ranging from changes in the local wind stress to the propagation of equatorially forced coastally trapped waves (strong during warm El Niño Southern Oscillation events; ENSO).

There is evidence that surface mesoscale eddies play an important role in the offshore transport of coastal waters, enhancing phytoplankton productivity offshore but their contribution still remains unclear. The use of satellite data and drifters to evaluate the offshore transport by surface eddies has indeed drawn significantly different conclusions. In particular, *Chaigneau and Pizarro* [2005] have reported that "about 2/3 of the vortices identified from drifter data are anticyclonic, whereas 2/3 of the long-lived eddies tracked from altimetry measurements are cyclonic." While the drifters' analysis is biased toward regions of convergence flow (e.g., anticyclonic eddies), the geostrophic flow derived from altimetry data lacks in the representation of small-scale processes and ageostrophic motions. The main eddy characteristics in the SEP include an offshore velocity varying from $\sim$3 cm s^{-1} (south of 30°S) to $\sim$6 cm s^{-1} (north of 15°S) and diameters up to 200 km [*Chaigneau and Pizarro*, 2005]. Consistent with the beta plane approximation theory, whereas

cyclonic eddies propagate westward, satellite derived long-lived anticyclone eddies propagate northwestward [*Chaigneau and Pizarro*, 2005; *Chelton et al*., 2011]. Drifters and satellite data however limit our understanding of eddy transport to surface eddies only and therefore leave us with an incomplete picture of the net offshore transport.

Below the surface the SEP circulation is dominated by the poleward Peru-Chile Undercurrent (PCUC). Originated at the equator, the PCUC develops at the continental slope between 100 and 400 m depth and is identified by the water mass characteristics of the Equatorial Subsurface Waters (ESSW) [*Gunther*, 1936; *Silva et al*., 2009]: subsurface salinity maximum (34.2–34.6), relatively warm, rich in nutrients and low oxygen concentrations (<3 mL L^{-1}). The instability of the PCUC has been observed to generate an ocean mesoscale eddy group known as "Intrathermocline eddies" (ITEs) [*Hormazabal et al*., 2013] or "equatorial Pacific 13°C Water Eddies" [*Johnson and McTaggart*, 2009]. Also named Cuddies (California Undercurrent eddies) for the California Current System or Meddies associated with the Mediterranean outflow, the SEP ITEs have an ESSW core within the thermocline and influence the intermediate and deep ocean layers. Unlike surface intensified eddies which can be characterized from satellite data only, ITEs have been able to be detected recently using Argo floats [*Chaigneau et al*., 2011; *Johnson and McTaggart*, 2009] or hydrographic data [*Morales et al*., 2012]. From oceanic cruises, *Hormazabal et al*. [2013] describe ITEs off Central Chile as follows:

1. Subsurface lenses of $\sim$100 km diameter and 500 m thick
2. Generally anticyclone
3. Nearly homogeneous salinity (>34.5)
4. Oxygen-deficient (<1.0 mL/L) waters
5. PCUC origin
6. Westward mean speed of $\sim$2 km/d
7. Offshore transport of $\sim$1 Sv
8. At least 5–7 ITE's were observed simultaneously between 31°S and 38°S.

This description is corroborated by an additional cruise collecting data off Central Chile at $\sim$ (77.5°W, 38°20'S) and illustrated in Figure 1. Density, Temperature, Salinity, and Dissolved-Oxygen profiles reveal that the cruise had crossed an ITE during 7–9th, 2005. Figures 1a–1c show that the top 600 m density profile of the ITE displays a lens shape centered at $\sim$200 m depth and a depression of the isotherms as deep as 600 m in the eddy core. Characteristic of ITEs, we also find that the most striking difference from the surrounding water is the high salinity (>34.5) and low dissolved oxygen (<0.5 mL L^{-1}) eddy core, signature of the ESSW (Figures 1b–1d).

Although observational studies provide an accurate description of the ITEs of the SEP, their statistics remains, however, unknown. For example, we do not know if there is a relation between the strength of the PCUC (source of the ITEs) and the ITEs statistics. It is also unclear how the equatorial signal affects the ITEs variability, even though *Hormazabal et al*. [2013] observe differences between ITEs identified from cruises carried out during one of the strongest El Niño events (1997) and during 2009 off central Chile. The goal of this study is to address the connection between ITEs, PCUC variability and the equatorial variability. We will use modeling experiments to address the net surface and subsurface offshore eddy transports and their relation to the equatorial dynamics over the period 1979–2012. This paper is organized as follows. Section 2 describes the model experiment. Section 3 describes the structure and characteristics of surface and subsurface eddies. Section 4 examines the variability of the PCUC. The variability of the eddy statistics is described in section 5. Section 6 is left for the conclusion.

2. Model Setup

The model used is the Regional Ocean Modeling System (ROMS) [*Shchepetkin and McWilliams*, 2005]. ROMS is a hydrostatic primitive equation model with terrain-following vertical coordinate and orthogonal curvilinear coordinates in the horizontal. The ROMS_AGRIF version (http://roms.mpl.ird.fr/) is chosen for its capability of a two-way nesting procedure [*Debreu et al*, 2011] in which a high-resolution "child" model is

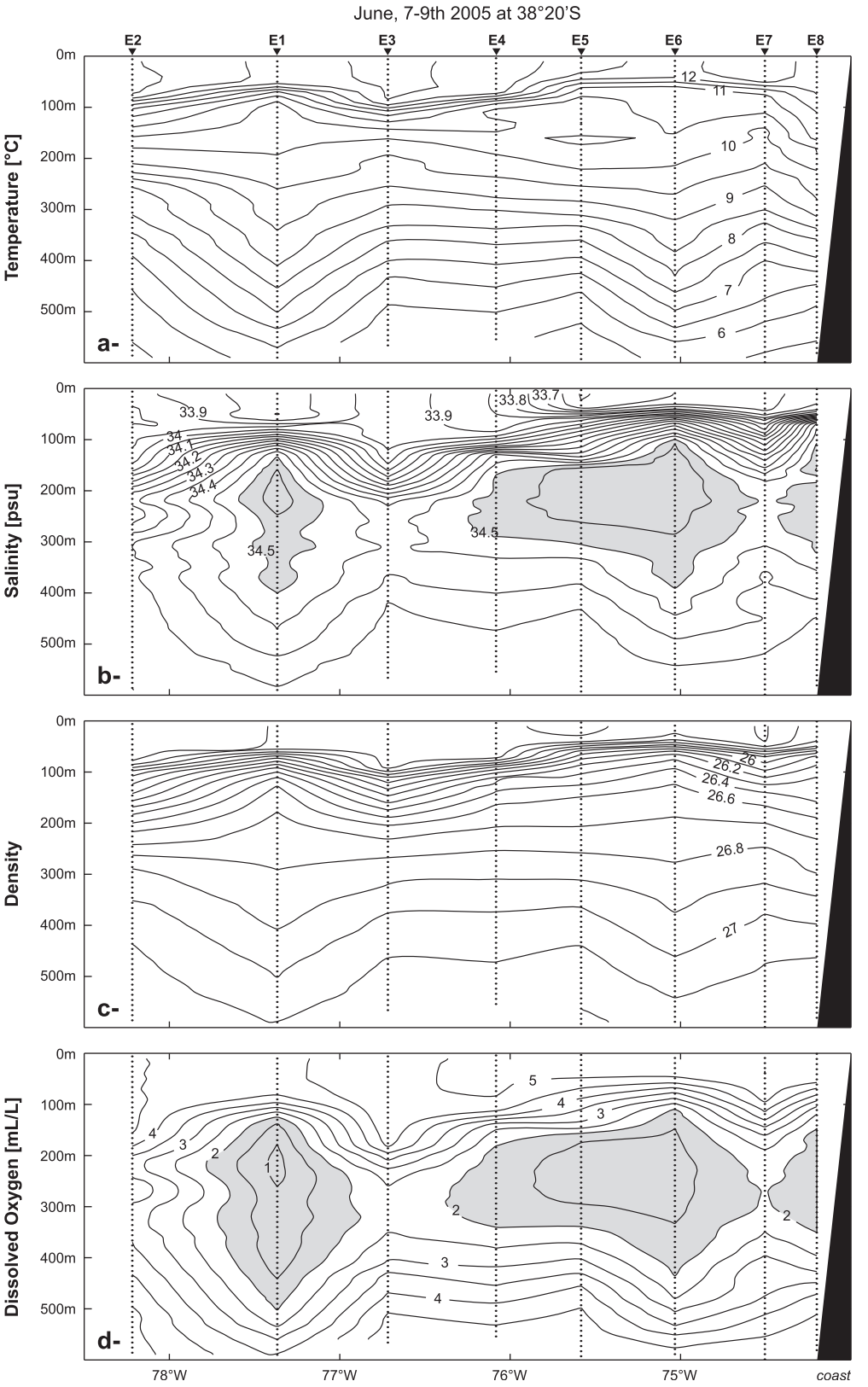

Figure 1. Cross-shore hydrographic sections during the oceanographic cruise carried out during 7–9 June 2005 at 38°20'S. Figures 1a–1d show respectively the temperature, salinity, density and dissolved oxygen.

Table 1. Correlation Coefficients of the Total Eddy Volume, Number of Eddies, and Mean Eddy Radius With the Nino3.4 Index[a]

	Total ITEs Volume	Number of ITEs	Mean ITEs Radius
5°S–46°S	**−0.48 *(260 d)***	**−0.42 *(310 d)***	−0.35 *(180 d)*
5°S–22°S	**−0.44 *(190 d)***	−0.25 *(230 d)*	**−0.40 *(150 d)***
22°S–46°S	**−0.45 *(330 d)***	**−0.41 *(330 d)***	−0.23 *(390 d)*

[a]The time series are anomalous time series computed for subsurface anticyclonic eddies found within 500 km from the coast and between 5°S and 46°S (first row). Second and third row separate eddies north and south of 22°S. The lag of maximum correlations is shown in parenthesis. Correlations above 99% confidence are shown in bold.

embedded into a coarser resolution "parent" model (Table 1). The parent grid extends 360° in the longitude and from Antarctica to 15.2°N (Figure 2). The parent grid has a spatial resolution of 1/4° and 40 vertical levels with enhanced resolution at the surface. The child grid covers the coasts of Peru and Chile, extends from 93°W to 71°W and from 47°S to 5°S and has a spatial resolution of 1/12° (Figure 2). For a bathymetry of 4000 m, the model has 12 vertical levels between 100 m and 600 m depths where ITEs propagate (the depths of the 12 vertical levels are 104, 121, 140, 162, 188, 218, 253, 294, 341, 395, 458, and 532 m). The bottom topography was derived from the ETOPO1 (1′ resolution) [*Amante and Eakins*, 2009]. To prevent horizontal pressure gradient errors [*Beckmann and Haidvogel*, 1993], bottom slopes were smoothed to meet the r-factor criterion of 0.20. The model equations are based on an upstream third-order advection scheme, in which the diffusion of tracers (Temperature and Salinity) is split from the advection term and where diffusion is represented by a biharmonic diffusivity satisfying the Peclet constraint [*Marchesiello et al*., 2009]. The model uses the KPP scheme for vertical mixing in the surface boundary [*Large et al*., 1994]. For more details, a similar model setup in which the child grid was applied to the Southwest Atlantic is described in *Combes and Matano* [2014].

At the surface, the model is forced by the ERA-Interim data set from 1979 to 2012 with a spatial resolution of 0.75° [*Dee et al*., 2011]. A bulk formulation [*Fairall et al*. 1996] derives the surface wind stress, heat, and freshwater fluxes from the 3 days averaged ERA-Interim 2 m air temperature, relative humidity, precipitation, 10 m wind amplitude, short wave, and long wave radiation. Because of large errors over coastal upwelling regions [*Röske*, 2006], we use climatology short and long wave radiation from the COADS data set [*Da Silva et al*., 1994]. A model experiment using short and long wave radiation from ERA-Interim (not shown here) has been performed and has indeed confirmed an unacceptable surface warming (compared to satellite sea surface temperature; SST). At the single open boundary of the parent grid (at 15.2°N), we impose a modified radiation boundary condition [*Marchesiello et al*., 2001] with nudging to the monthly mean climatology provided by the Simple Ocean Data Assimilation model (SODA) [*Carton and Giese*, 2008]. The SODA model also provides the initial condition. The parent grid had first spun up for 10 years (with climatological surface forcing) followed by a 5 years model integration of the nested configuration. The key advantage of the nesting procedure, in which the parent model provides the boundary conditions for the child at each baroclinic time step, is to allow the equatorial Kelvin waves (generated in the parent grid) to propagate into the high-resolution child grid.

The transport pathways and statistics associated with the mesoscale circulation are characterized using a passive tracer advection-diffusion equation that is identical to that used for the temperature and salinity fields. Two independent tracers are continuously released in the model domain to track coastal water masses. The "surface-released Tracer" is released from the coast to 50 km offshore and from the surface to 50 m. The "subsurface-released Tracer" is identical as the surface-released Tracer but released between 300 m and 150 m depth (within the core of the PCUC). Note that all analyses are based on a 10 days averaged model output.

To illustrate the model configuration, Figure 2 shows a snapshot of the model SST for 4 June 2000. Described in *Combes and Matano* [2014], the large-scale circulation shows a good agreement with observations. At the coast, the model results exhibit two main coastal upwelling regions located off Peru and Central Chile (Figure 2), consistent with satellite mean SST (dashed grey contours). The equatorial upwelling and its instability are also apparent in the SST of the coarse (1/4°) parent grid. To verify that the model captures the equatorial variability, we compare the anomalous (seasonal variability removed) depth of the 20°C isotherm at (110°W, 5°S) and the Niño3.4 index (Figure 2). The correlation is high and significant ($R=-0.82$).

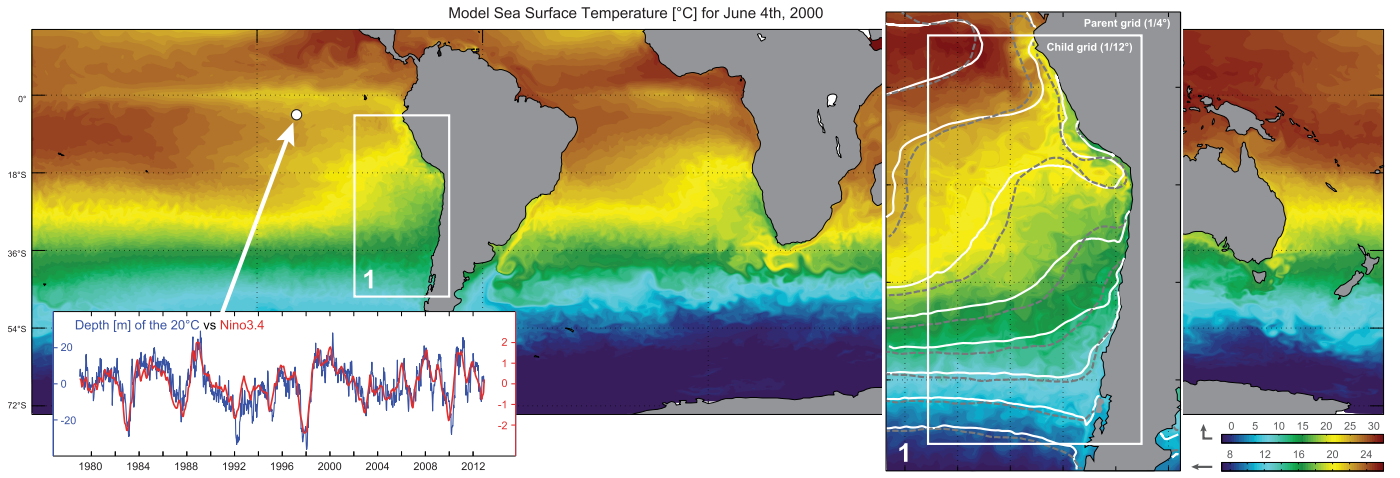

Figure 2. Snapshot of the model Sea Surface Temperature (SST) for 4 June 2000. White (dashed gray) contours correspond to the mean model (PathFinder satellite) SST. The bottom left inset compares the anomalous (from the seasonal cycle) depth of the 20°C at (110°W–5°S; blue) and the Nino3.4 index (red).

To validate the coastal variability of the model solution and illustrate its connection to ENSO along the coasts of Peru and Chile, Figure 3a compares the model sea level height (SSH) with available in situ records at eight different locations (provided by the University of Hawaii Sea Level Center http://ilikai.soest.hawaii.edu/uhslc/data.html): Lobos de Afuera (6°56′S), Callao (12°03′S), Pisco (13°25′S), San Juan (15°22′S), Arica (18°28′S), Antofagasta (23°39′S), Caldera (27°04′S), and Valparaiso (33°02′S). With more than 10 years of in situ data, each coastal station captures strong warm ENSO events. The model coastal SSH explains a significant fraction of the in situ sea level variance with strong positive anomalies during the warm ENSO events of 1982 and 1998 (El Niño years). Those strong anomalous SSH are associated to the propagation of coastally trapped Kelvin waves originated at the equator (Figure 3b). For example, during 1997–1998, the Hovmöller diagram in Figure 3b illustrates two strong downwelling Kelvin waves propagating first along the equator and then along the coast as south as 40°S at a mean velocity of ∼2–4 ms^{-1}. Over the period 1979–2012, both in situ and model SSH at Lobos de Afuera (Peru) have a maximum spectral density at ∼40–60 days, 1 year and ∼4–5 years. At the intraseasonal band (40–90 days), it is noteworthy mentioning that previous studies have shown that the SST variability is principally attributed to local winds and heat fluxes rather than to equatorial forcing (even off Peru). Off central Peru, *Illig et al.* [2014] show that the remote equatorial forcing only accounts for ∼20% of the intraseasonal SST variability.

Over the deep ocean, the model SSH (SSHa) anomalies also compare relatively well with altimetry data for the period 1993–2012 (Figure 4), where the anomalies are defined by removing the seasonal cycle. The spatial structure of the first mode of model SSHa (EOF1; Figure 4b), which corresponds to a monopole with maximum off Peru, is similar to the EOF1 of satellite SSHa (Figure 4a). The variability of the model SSHa EOF1 (PC1; Figure 4e) is highly correlated with the PC1 of the satellite SSH (0.79) with strong signal during the 1997–1998 El Niño event. Although the second mode of variability of satellite and model SSHa explains only 10% and 15% of the SSHa variance respectively, the model SSHa compares well with satellite SSHa variability. Both EOF2 (Figures 4c and 4d) correspond to a dipole with maximum off Peru and minimum off Chile and their variability (PC2) are highly correlated (Figure 4f).

Throughout this study, the eddy field will be described both at the surface and in the subsurface. While the word "surface" will indicate the upper-most model vertical layer, the term "subsurface" will refer to the depth of the 1027.5 isopycnal, which is chosen because it crosses the PCUC at the coast. The spatial structure of the depth of the 1027.5 isopycnal compares well with observation (Figure 5). This isopycnal is generally shallow at the coast and deepens offshore. Note that subsurface eddies (or ITEs) generated at the coast will, therefore, sink as they move westward within the thermocline [*Hormazabal et al.*, 2013].

At the surface, the amplitude and spatial structure of the model mean Eddy Kinetic Energy (EKE) compares relatively well with satellite altimetry derived EKE (Figures 6a and 6b). Both model (1/12° resolution) and altimetry (1/4° resolution) show maxima in the northern Peru (north of 12°S), central Peru (13.5°S–18.5°S)

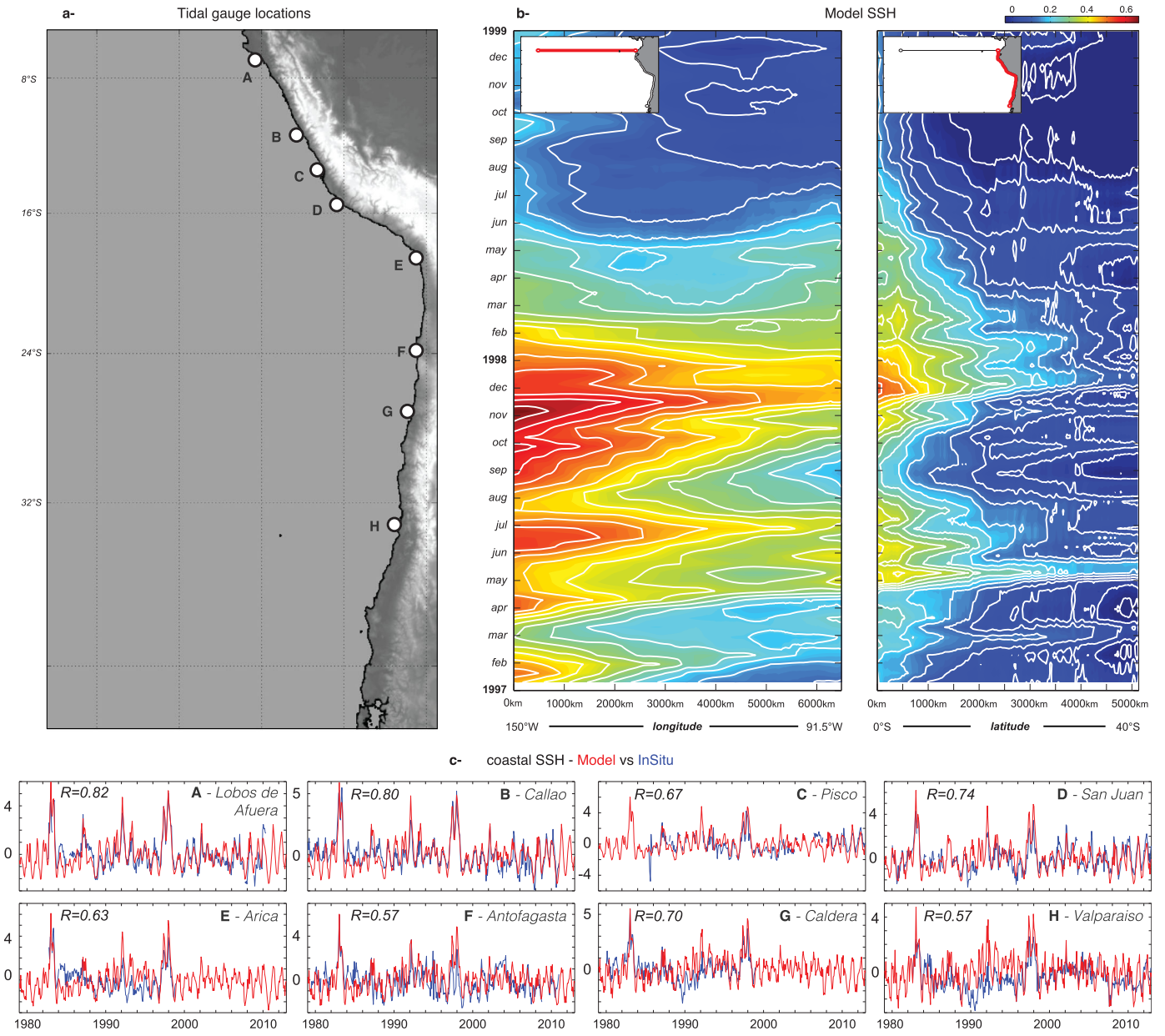

Figure 3. (c) Comparison of model (red) and in situ (blue) monthly coastal SSH at eight different locations along the coasts of Peru and Chile indicated in Figures 3a and 3b shows a Hovmuller diagram of model SSH along the equator and along the coasts of Peru and Chile, during the period 1997–1999.

and off central Chile (27°S–39°S) and minima off northern Chile (18.5°S–22.5°S) and coastal central Chile. Off central Chile, the offshore location of the maximum EKE is due to the instability of an oceanic jet, which develops during spring and summer north of Punta Lavapie (∼37°S) and associated with the presence of a low-level wind jet [*Aguirre et al*., 2012]. Below the surface (at the depth of the 1027.25 isopycnal), the mean EKE (computed from model currents) is slightly different from the surface mean EKE (Figure 6c). Off central Chile, for example, the subsurface EKE show maximum value at the coast, resulting from the instability of the PCUC.

3. Eddy Characteristics

Several methods have been developed for detecting eddies. The most popular ones are based on SSH [*Chaigneau and Pizarro*, 2005; *Chelton et al*., 2011] or OkuboWeiss Parameter (Q) contours [*Isern-Fontanet*

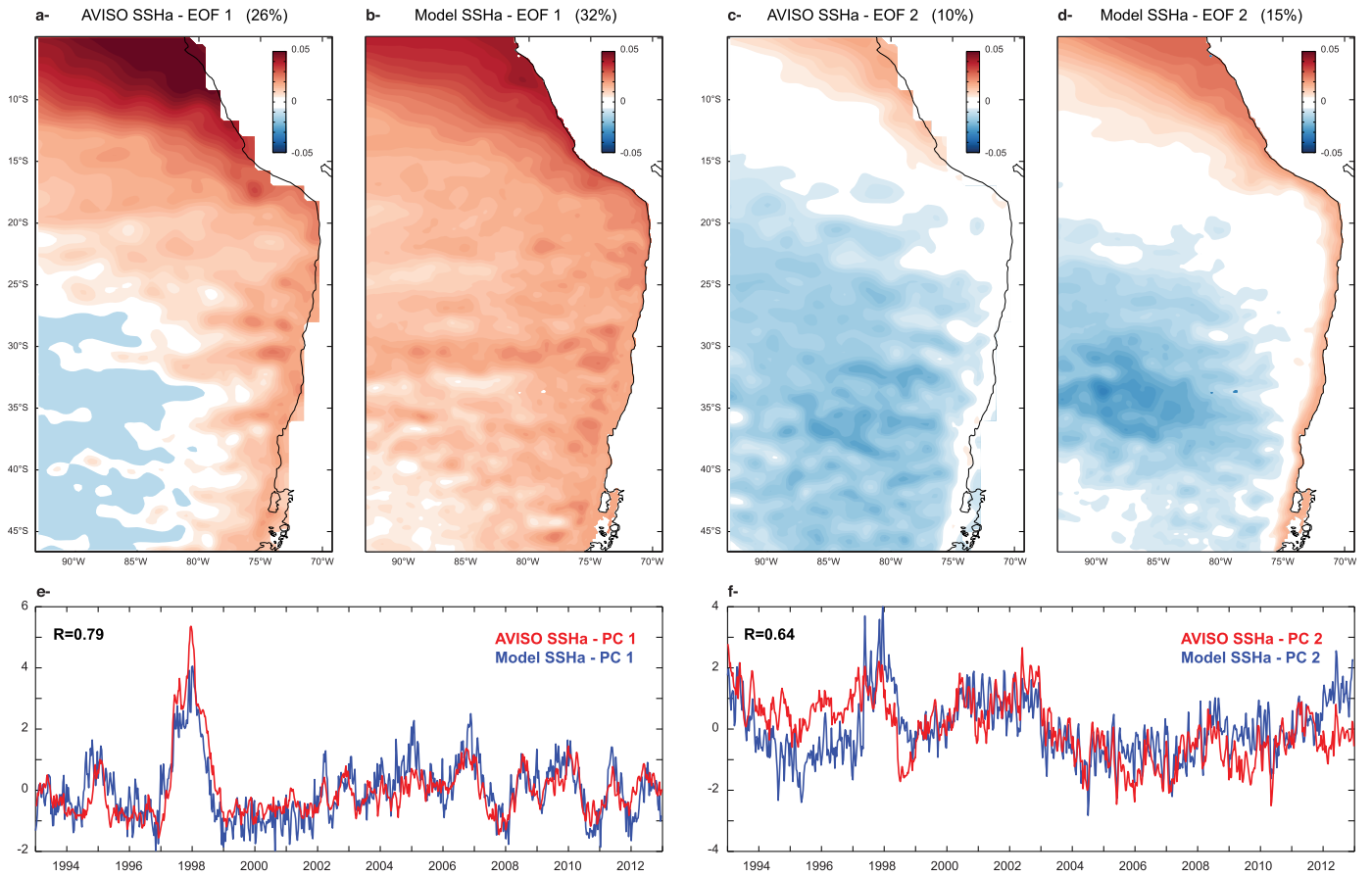

Figure 4. First and second Empirical Orthogonal Functions (EOF) of (a–c) satellite and (b–d) model sea surface height anomalies (from the seasonal cycle). The first and second Principal Components (PC) are shown in Figures 4e and 4f. Model SSHa PCs are shown in blue, Satellite SSHa PCs are shown in red.

et al., 2006]. Here we use the Q contours and follow a similar eddy detection method used by *Kurian et al*. [2011] applied on the eddy field of the California Current System. The Q field, defined by $Q=\left[\frac{\partial u}{\partial x}-\frac{\partial v}{\partial y}\right]^2+\left[\frac{\partial v}{\partial x}+\frac{\partial u}{\partial y}\right]^2-\left[\frac{\partial v}{\partial x}-\frac{\partial u}{\partial y}\right]^2$, is first smoothed using a two-dimensional Hanning smoother to reduce the Q noise. The closed contour searched is the -1×10^{-11} s^{-2} contour (∼mean standard deviation). Each closed contour must also pass a shape test described in *Kurian et al*. [2011]. To be accepted as eddy, the eddy shape-error (anomaly from a perfect circle) of the closed contour is chosen to be below 40%. Finally, only eddies with minimum radius of 0.2° are considered. The vorticity sign is used to differentiate cyclones from anticyclones. As mentioned in section 2, eddies will be analyzed both at the surface and along the 1027.5 isopycnal. A deep eddy can, however, pass the eddy criteria both at the surface and along the 1027.5 isopycnal. To avoid double counting, we separate surface-intensified from subsurface-intensified eddies using the vertical structure of Q at the eddy center. If the minimum of Q is above 50 m, the eddy is characterized as surface-intensified eddy: If the minimum of Q is found between 100 m and 300 m depth, the eddy is counted as subsurface-intensified eddy.

Eddy tracks are shown on Figure 7, which only shows eddy trajectories from 2000 to 2012 and with displacement over 2° for clarity. The most striking difference is in the asymmetry between surface and subsurface fields. While the long-lived tracked eddies are mostly cyclonic at the surface, the subsurface eddies are mainly anticyclonic. This asymmetry has also been noticed in the modeled long-lived eddies of the California Current System [*Kurian et al*., 2011]. It is however important to note that the eddy tracking is based on a 10 days averaged model output. Visual inspection shows that some rapid eddy can cross long distance in 10 days, and thus are considered as two different eddies in the tracking method. The eddy count over the period 1979–2012 confirms the strong preference of subsurface eddies to be anticyclone, with 27,384 surface cyclonic eddies, 22,745 surface anticyclonic eddies, 11,476 subsurface cyclonic eddies, and 21,707

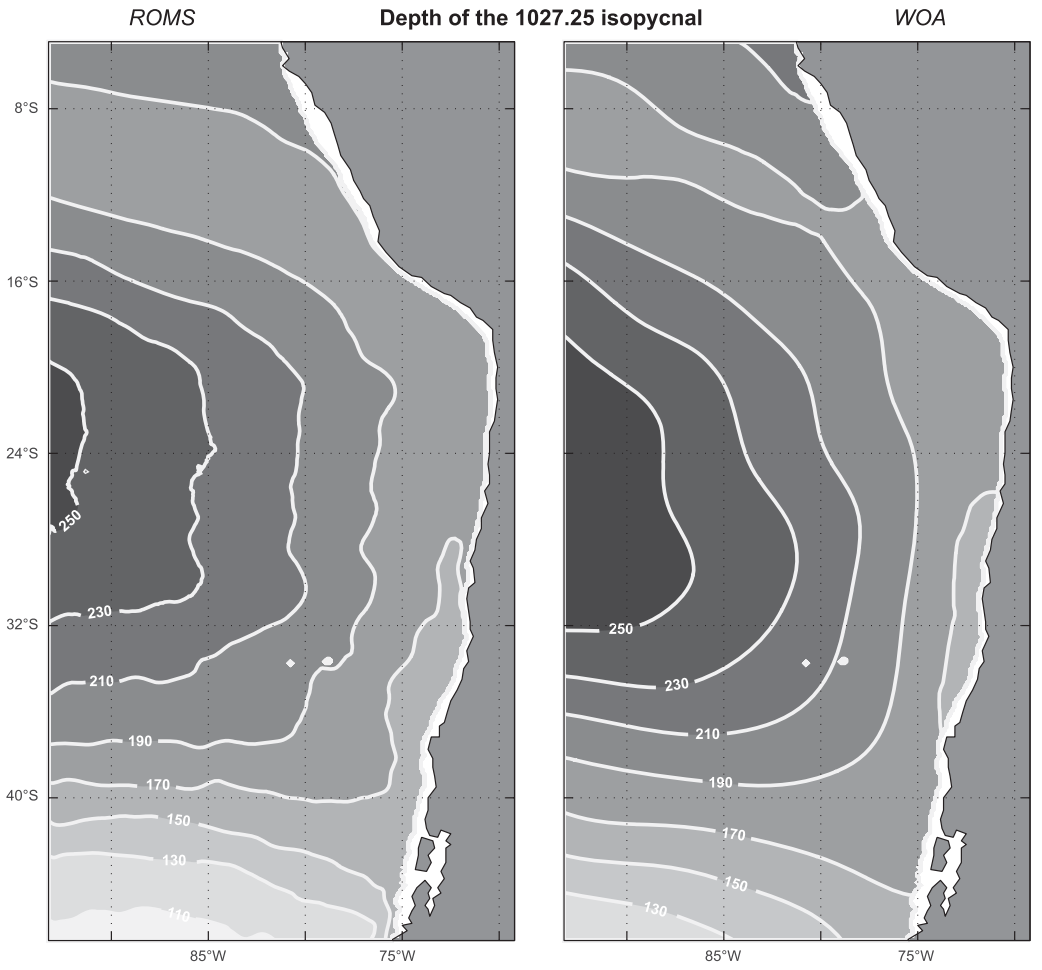

Figure 5. Depth (m) of the 1027.25 isopycnal derived from the model (ROMS) and the World Ocean Atlas (WOA).

subsurface anticyclonic eddies. Each group of eddies exhibits a strong tendency for westward propagation. As noted from altimetry-tracked eddies [*Chelton et al.*, 2007, 2011], anticyclones (77% of subsurface anticyclones) are also associated with a clear equatorial deflection.

Although observations give a good description of selected ITEs, their properties such as diameter, thickness, ESSW transport, or lifetime may change significantly among them [*Hormazabal et al.*, 2013]. To provide a general description of both surface and subsurface eddies, Figure 8 shows a composite of vorticity, temperature, salinity, and tracer concentration for all model eddies detected from 1979 to 2012 (27,384 surface cyclones, 22,745 surface anticyclones, 11,476 subsurface cyclones, and 21,707 subsurface anticyclones). The term "anomaly" in the composite analysis corresponds to the anomaly relative to the longitudinal trend (75 km east and west from the eddy center) for each depth. Surface intensified eddies (1st and 2nd column) have maximum vorticity at the surface and extend down to 300–400 m depth. Both cyclonic and anticyclonic subsurface eddies (third and fourth column) have a maximum vorticity around 150–200 m which corresponds to the mean depth of the PCUC and is consistent with observations (Figure 1). The core of surface eddies is generally cooler for cyclones and warmer for anticyclones, associated with the suppression and depression of the isotherms within the respective eddies. The cores of subsurface cyclones and anticyclones are also respectively cooler and warmer. The anomalous warm temperature of the ITEs is found below 100 m and as deep as 500 m. The salinity anomaly is particularly high within anticyclone subsurface ITEs, with a clear high salinity core centered around 200 m depth (consistent with observed ITE, Figure 1). Because the gradient of the background vertical salinity is high between 100 m and 200 m, the anomaly (white contours) is found ∼150 m.

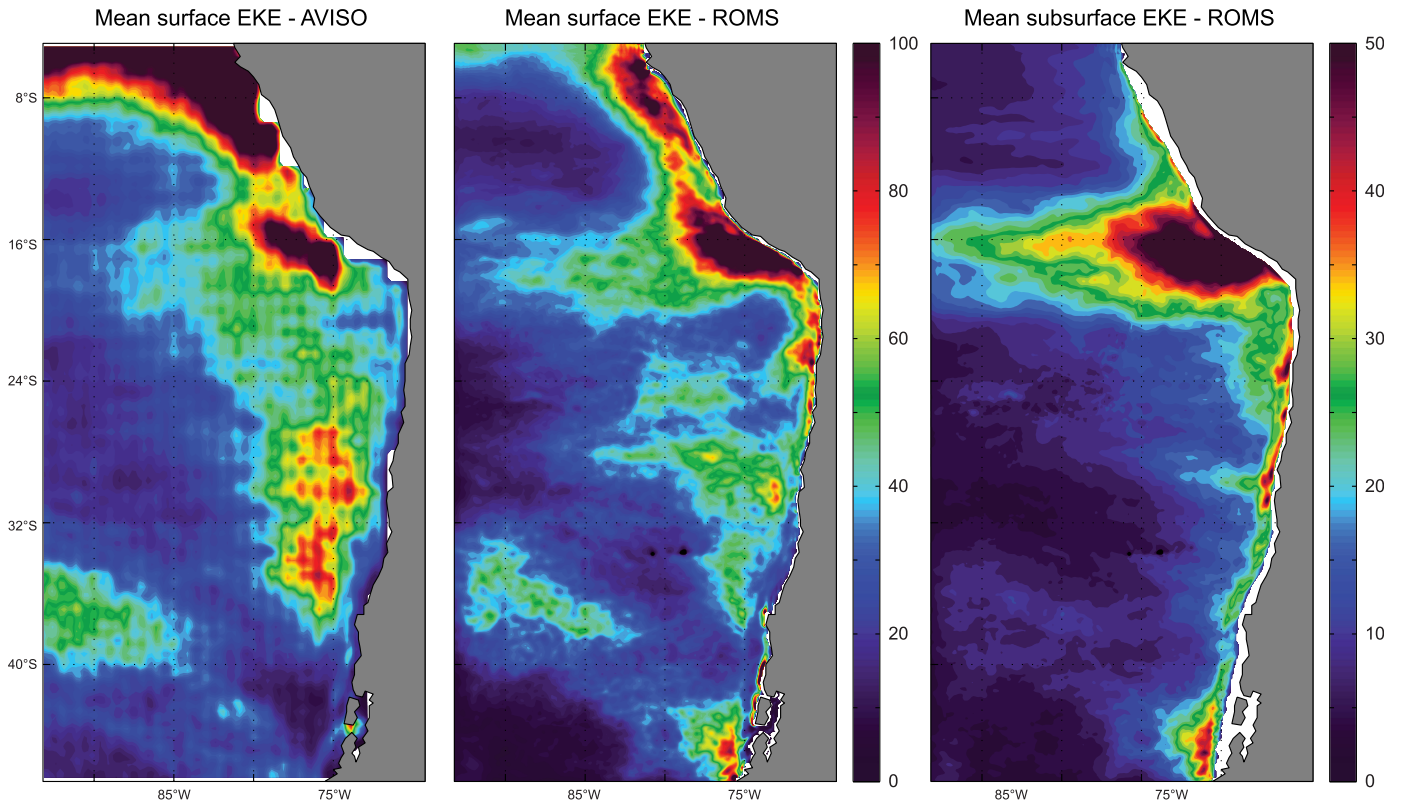

Figure 6. (a) Mean satellite surface EKE, (b) mean model EKE, and (c) mean model subsurface EKE in cm^2/s^2.

The transport of coastal surface and subsurface waters by mesoscale eddies is inferred respectively by the composite analysis of the model surface-released (fourth row) and subsurface-released (fifth row) passive tracers. We find that the surface cyclones transport positive anomaly of surface-released tracers while surface anticyclones transport negative anomalous concentration. Note that the maximum tracer anomaly seems to appear ∼10 km west of the surface cyclones centers. This offset can be explained by the vertical velocity across the surface cyclones; which is maximum ∼10 km east of the surface cyclones centers at 90 m depth (composite not shown). The anomalous positive (negative) vertical velocity east (west) of the eddy centers therefore advects upward (downward) low-concentration tracer (high-concentration tracer). The subsurface-released tracer anomaly is particularly strong within subsurface anticyclone eddies (ITEs); which are the main contributor to the offshore advection of coastal subsurface water. The use of model passive tracer confirms the high salinity core across the ITEs, originated in the PCUC. Note that surface cyclones also transport subsurface-released tracer at the surface. We find that part of the tracers is first upwelled at the coast and then advected offshore by surface cyclones (as for the surface-released tracer). To summarize, the modeled ITEs (Figure 8, fourth column) are consistent with observed ITEs (Figure 1). The averaged of 21,707 modeled ITEs is associated with a 150–200 m maximum vorticity, warm and saline core originated in the PCUC (subsurface-released tracer composite), characteristic of the ESSW.

The vertical structure of eddies presented above is consistent with the model study by *Colas et al.* [2012] and the study of *Chaigneau et al.* [2011] that uses Argo float profiles off Peru and Chile. Both studies show that cyclonic eddies are predominantly surface intensified, while anticyclonic eddies are associated with temperature and salinity anomalies centered between 200 m and 400 m depth. Note that the westward shift of the maximum surface tracers from the core of surface-intensified cyclones is also observed in the temperature vertical profile (Figure 8). Although we use a different eddy-tracking method than *Chaigneau et al.* [2011], both studies show a slight tilt in the temperature vertical structure, which add confidence in the degree of realism of the model solutions. The temperature minimum anomaly seems to be located west of the eddy center above 150 m and detected east of the eddy center below 150 m depth. It is noteworthy

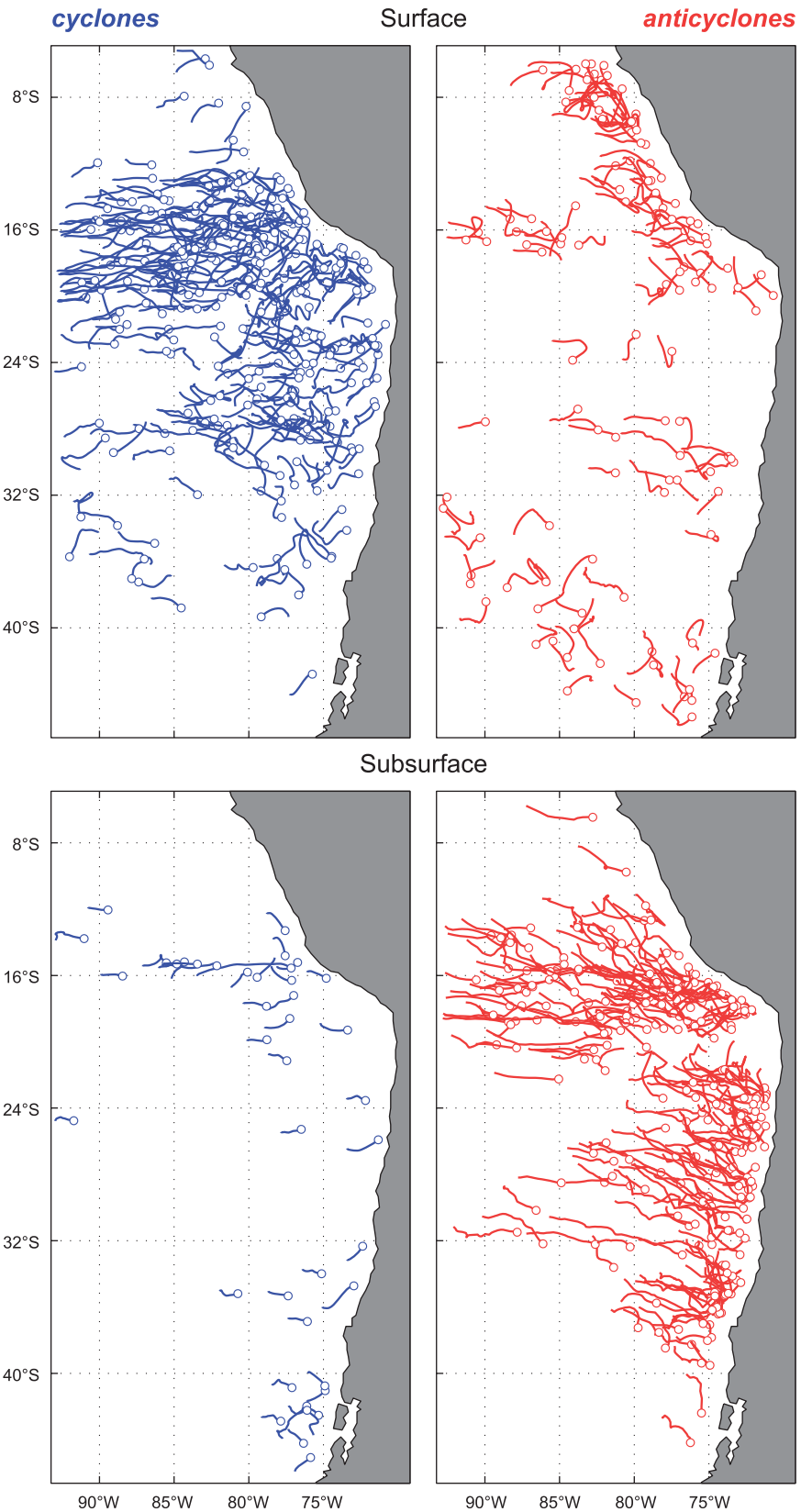

Figure 7. Track of long-lived eddy (distance >2°) from ROMS.

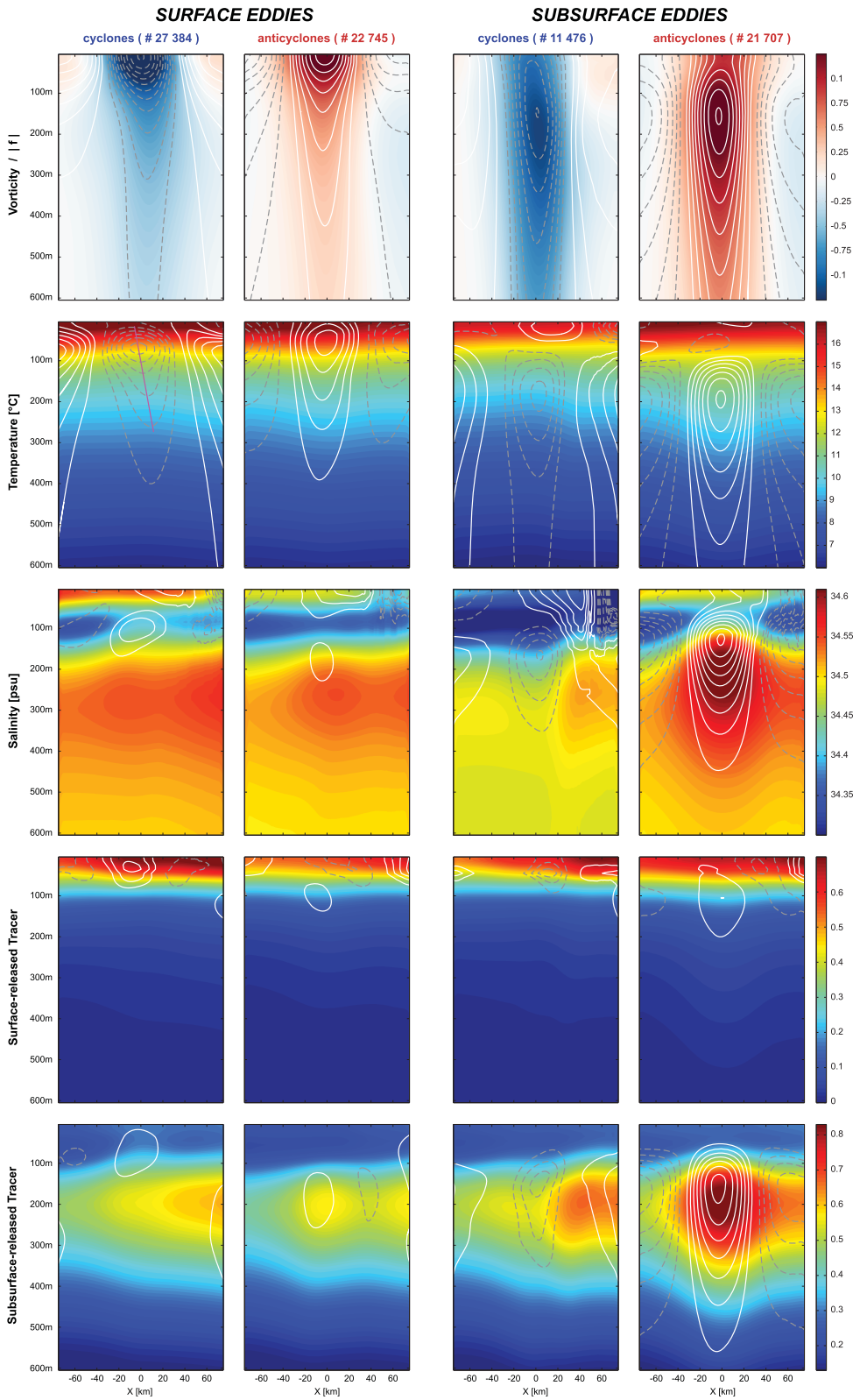

Figure 8. Composite maps of vorticity/f (1st row), temperature (second row), salinity (third row), surface-released tracer (fourth row), and subsurface-released tracer (fifth row). White contours (dashed gray) show the positive (negative) anomaly relative to the longitudinal trend (75 km east and west from the eddy center). X is the west (negative) and east (positive) distance relative to the eddy center. Contour intervals are 0.05°C for temperature anomaly, 0.01PSU for salinity anomaly, 0.02 for the subsurface-released Tracer concentration anomaly, 0.01 for the surface-released Tracer concentration anomaly and 0.01 for the vorticity anomaly.

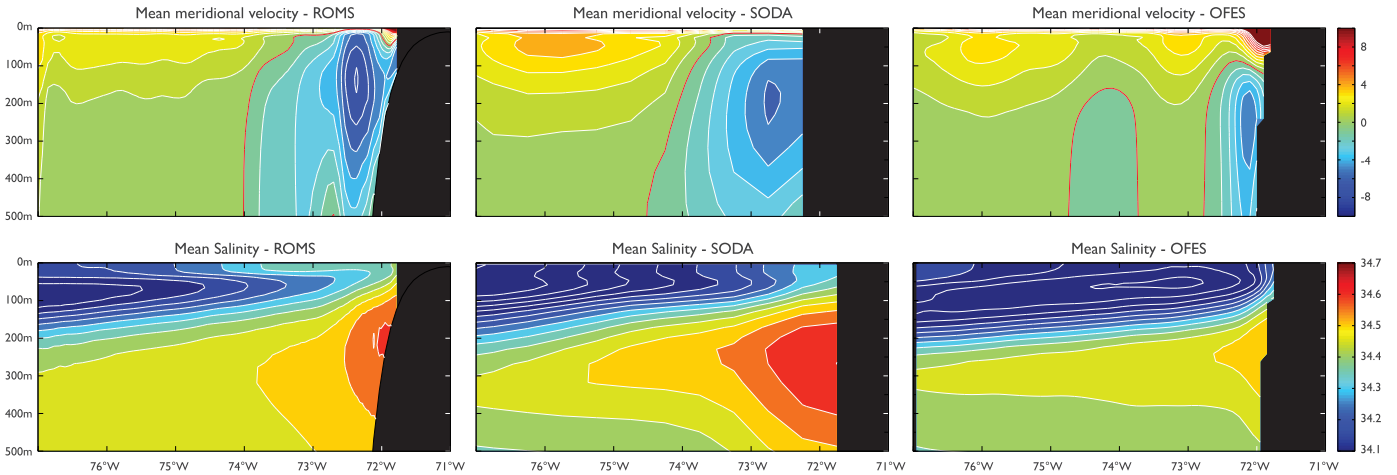

Figure 9. First row shows the mean merdional velocity from ROMS, SODA, and OFES at 33.25°S in cm/s. Contour interval is 1 cm/s. Red contour indicates the 0 cm/s contour. Second row compares the mean salinity from ROMS, SODA and OFES at 33.25°S (psu). Contour interval is 0.05 psu

of mentioning that based on recent numerical simulations [*Kurian et al*., 2011; *Colas et al*., 2012], our study corroborates that surface and subsurface mesoscale eddies in the Peru Chile Current System show similar characteristics to those of the California Current System where the California Undercurrent acts as the PCUC.

4. Variability of the PCUC

The presence of a subsurface poleward flow along the Pacific coast of South America was first reported by *Gunther* [1936], transporting ESSW as south as 48°S [*Wooster and Gilmartin*, 1961; *Silva and Neshyba*, 1979]. Off Peru, the observed mean PCUC flow is ∼5–10 cm s^{-1} [*Huyer et al*., 1991] and 12–13 cm s^{-1} at 30°S off Chile [*Shaffer et al*., 1999]. To assess the skill of the model to reproduce the PCUC, we compare the model mean meridional velocity and salinity with the ones from the data-assimilation SODA model and the global 0.1° resolution OFES model [*Masumoto et al*., 2004; *Sasaki et al*., 2004, 2008] at 33.25°S (Figure 9). The model meridional velocity shows a reasonably good agreement with the SODA/OFES solutions, with, however, some noticeable differences. First, we notice a stronger mean PCUC velocity compared to SODA and OFES, but it however underestimates the estimate from *Shaffer et al*. [1999]. Second, the ROMS PCUC core also appears to be shallower (∼150 m) and slightly offshore than in SODA and OFES, which can be attributed to the degree of realism of the costal wind stress. *Cambon et al*. [2013] present a number of sensitivity experiments to different wind stress products. The latter study shows in particular that the position of the PCUC is highly sensitive to the mean wind stress. For example, they show that while the PCUC is ∼200 m deep in a model experiment forced by QuickSCAT wind stress (the most realistic case) [*CERSAT*, 2002], the PCUC core is, however, located around 50 m when the model is forced by NCEP/NCAR (National Centers for Environmental Prediction and the National Center for Atmospheric Research) [*Kanamitsu et al*., 2002] wind stress. Finally, the nearshore surface northward current (Figure 9) also seems to be shallower compared to the one from OFES or to the different model experiments described in *Cambon et al*. [2013]. Note that few degree south (37.5°S; not shown), the nearshore current is 100–150 m deep with mean value greater than 0.12 m/s, consistent with *Cambon et al*. [2013]. The model salinity profile at 33.25°S also shows a good agreement with the SODA salinity, with a maximum salinity around 200 m depth. We have noticed that the presence of the PCUC salinity maximum at this latitude highly depends on the model advection scheme. The advection scheme proposed by *Marchesiello et al*. [2009], used in this study, prevent from strong spurious diapycnal mixing over steep bathymetry slopes. A comparison with a model solution without the correction proposed by *Marchesiello et al*. [2009] reveals that although the meridional velocity of the PCUC is comparable, the PCUC core is not anymore associated with a salinity maximum. Throughout this section, we define the PCUC transport (latitudinal dependent) as the meridional transport across the 3 cm s^{-1} contour within 150 km from the coast and above 700 m depth.

The PCUC transport variability is illustrated in Figure 10. Note that the PCUC transport power spectrum has a latitudinal dependence (Figure 10a). While the high frequency (40–60 days) signal is consistent off Northern Chile (25°S–20°S) and central Chile (36°S–31°S), the seasonal variability is strongly different. The PCUC transport off northern Chile has little energy at the annual cycle, whereas it has a strong seasonal variability off central Chile (Figure 10c) where the meridional wind stress seasonality is also maximum (Figure 10a). Although the meridional wind stress has a marked annual oscillation with only one maximum during November (not shown), the PCUC also exhibits a semiannual signal with poleward maxima during May and December (between 36°S and 31°S). The second PCUC minimum during March originated at lower latitude, where a similar amplitude (∼1 Sv between March and May) is also observed off northern Chile in March (Figure 10b). Previous studies have observed a similar behavior of the thermocline variability. Based on hydrographic data at ∼21°S, *Ramos et al*. [2006] also find that while the annual thermocline signal is linked mainly to surface wind stress, the semiannual component has an equatorial origin. The thermocline being shallower (deeper) during March–April (June) and August–September (December). The interannual PCUC transport variability averaged from 25°S to 20°S is illustrated on Figures 10d and 10e. The PCUC time series, which has a mean value of 2.7 Sv between 1979 and 2012 and standard deviation of 1.7 Sv, exhibits a strong interannual variability. In particular, the PCUC is maximum during 1997 (∼16 Sv) and 1998 (∼10 Sv), which are in phase with the presence of downwelling Kelvin waves originated in the Equator and propagating along the Peruvian and Chilean coasts (SSH; Figure 3). Although the correlation between the Niño 3.4 index and the PCUC transport is low between 2003 and 2012 (R=0.05 for the time series on Figure 10e), the relation is higher during the period 1979–2003 (R=0.58 for the time series on Figure 10e with a 120 days lag). In particular, the model output shows a strengthening of the PCUC transport during strong El Niño events. Note that this is also supported by *Montes et al*. [2011], who reproduce a larger PCUC transport during the 2002–2003 El Niño event compared to the 1999–2000 La Niña event using modeling experiments.

Based on coastal sea level, current, satellite altimeter data and analytical model, *Pizarro et al*. [2002] have examined the variability of the PCUC. In particular, they found that "more than 50% of the observed undercurrent variability near 30°S, at seasonal and interannual periods can be explained by long Rossby waves forced by the equatorial Kelvin waves" [*Pizarro et al*., 2002]. This is in agreement with Figure 10c and supports the equatorial origin of the secondary PCUC transport minimum observed in March. Note that in *Pizarro et al*. [2002], the PCUC is defined as the alongshore velocity at 220 m depth from a slope mooring near 30°S. Their in situ PCUC alongshore velocity over the period 1993–1999 does, however, not exhibit a significant strengthening during the strong 1997–1998 El Niño event, unlike the transport shown on Figures 10d and 10e. It is noteworthy mentioning that using the same definition as in *Pizarro et al*. [2002], we find that the model alongshore velocity also does not display a significant strengthening during strong El Niño events (as in Figures 10d and 10e). We therefore argue that the meridional velocity at 220 m over the slope at 30°S does not represent the net PCUC transport which also suggests that the location of the PCUC core may vary spatially.

5. Subsurface Eddy Statistics

The model solution indicates that the number of subsurface eddies shows a significant year-to-year variability. For example, we identify 32 subsurface eddies during November 1983 while 77 eddies are detected during June 2011 (Figures 11a and 11b). We will examine the interannual variability of the eddy statistics and address the connections between ITEs, PCUC variability and the equatorial variability. To account for the size of the eddies, we examine the variability of the volume of subsurface eddies found within 500 km from the coast, rather than the variability of the number of eddies (Figures 11a and 11b). While the radius is inferred from the eddy detection method (section 3), the eddy thickness is defined as the vertical distance between the 1026.7 and 1028.5 isopycnals (two isopycnals that envelop the mean PCUC). The following results however do not change significantly if we change those two arbitrary isopycnals values, since the thickness (O(100 m)) is much smaller than the radius square of the eddies (O(10^2 km)). The variability of the total eddy volume is illustrated in Figure 11c. One might expect that as the PCUC transport increases during El Niño years (described in the previous section), more eddies will be triggered and detached from the PCUC at that time. The model solution, however, shows an opposite behavior with significantly less eddies identified during strong El Niño years. In fact, Figure 11c indicates that there is an inverse relationship between the volume of subsurface eddies and the Niño3.4 index (R=−0.47; lag 250 days). The lag of 250

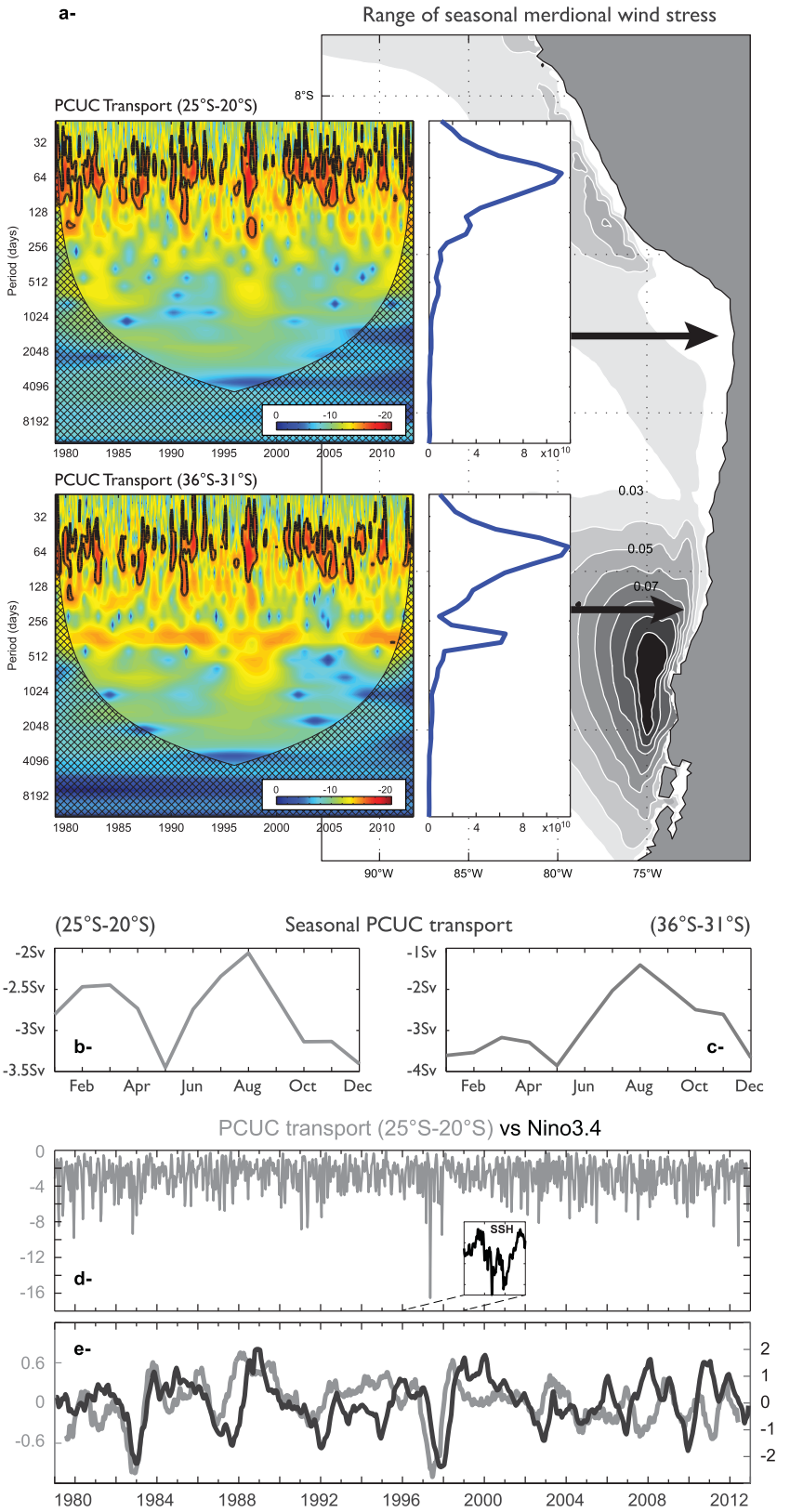

Figure 10. (a) Wavelet power spectra and time-averaged wavelet power spectra for the PCUC transport averaged between 25°S–20°S (top wavelet) and 36°S–31°S (bottom wavelet). Right-hand side figure shows the range of the seasonal meridional wind stress. Contour interval is 0.01 N/m^2. (b, c) Seasonal PCUC transport averaged between 25°S–20°S and 36°S–31°S. (d) The PCUC transport from 1979 to 2012 (gray in Sv) and the SSH from 1996 to 1999 (black). (e) Comparison of 1 year lowpass PCUC transport anomaly and the Niño 3.4 index.

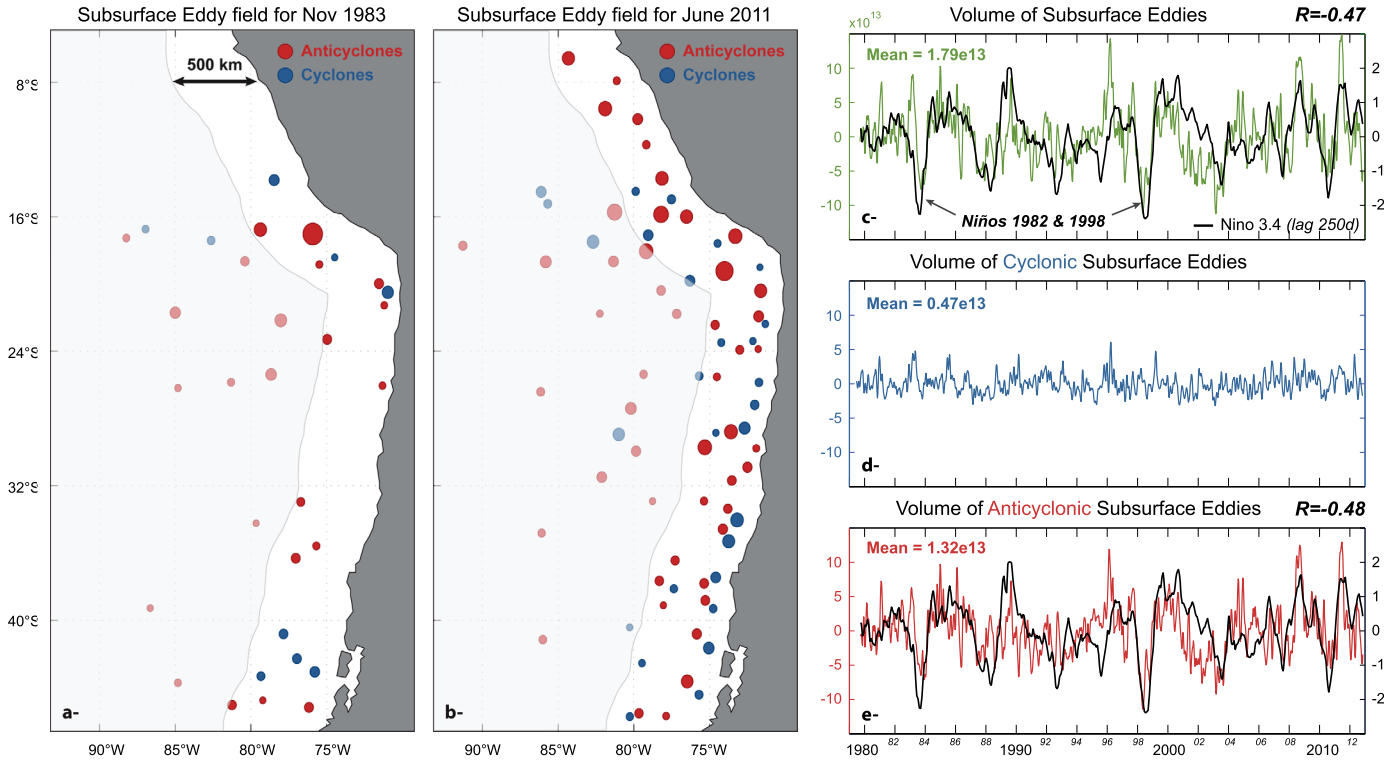

Figure 11. Snapshot of the subsurface Eddy field for (a) November 1983 and (b) June 2011. The green time series shows the variability of the volume of subsurface eddies within 500 km from the coast. The volume of cyclones and anticyclones are represented by the blue and red time series. The Niño3.4 index is shown in black. Green, blue and red time series are 40 days lowpassed (unit: m^3).

days corresponds approximately to the time for eddies to cross the 500 km coastal region at ~2 km/d, which is also the estimation observed in *Hormazabal et al*. [2013]. We also find that it is the anticyclones (ITEs; Figures 11d and 11e) that explain most of the total eddy volume variability. The correlation slightly increases (R=−0.48) when considering the ITEs variability only. It is also noteworthy mentioning that the contributions of the Eddy radius and Eddy count to the Eddy volume variability are different off Peru (5°S–22°S) and off Chile (22°S–46°S). Off Peru the ITEs radius variability accounts for the largest fraction of the correlation with the Niño3.4 index, while off Central Chile the correlation is dominated by the ITEs counts (Table 1).

To explore the source of the inverse relationship between ITEs and the equatorial signal (Niño3.4 index), we first explore the changes of subsurface EKE between El Niño (Figure 12a) and La Niña (Figure 12b) periods. Consistent with the strengthening of the PCUC transport during strong El Niño events, the model subsurface EKE increases along the coast (Figure 12a). Few kilometers offshore (of Peru and Chile; Figures 12a and 12b) the EKE, however, decreases during El Niño events which becomes consistent with the inverse relation found between the volume of subsurface eddies and the Niño3.4 index (Figures 11c–11e). The weakening of the EKE offshore, and therefore, the decrease of the number of ITEs is consistent with a weakening of baroclinic instability caused by the relaxation of the isopycnals along the coast during El Niño events (deepening of the isopynals; black contours on Figures 12a and 12b). Inversely, during negative Niño3.4 index (La Niña events), the 1027.25 isopycnal depth is shallower at the coast (higher zonal density gradient) which leads to an increase of subsurface EKE (Figures 12c and 12d) and therefore to an increase of the subsurface eddy transport.

6. Conclusions

We discuss the results of a ROMS high-resolution (1/12°), nested simulation of the Southeast Pacific circulation in which we released model passive tracers to track coastal surface and subsurface waters. A comparison between model results and observations indicate that the model reproduced the main regional

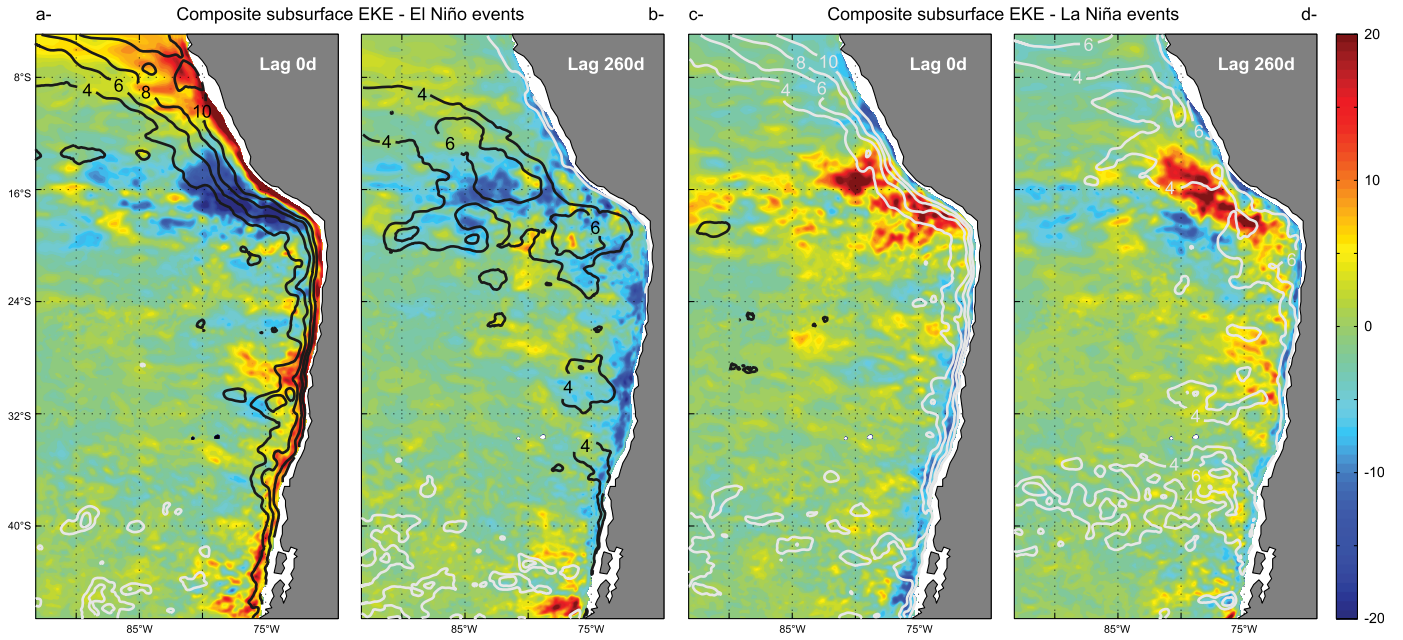

Figure 12. Composite maps of model subsurface EKE anomaly for (a–b) high and (c–d) low Nino3.4 index in cm^2/s^2. Contours indicate the anomalous depth of the 1027.25 isopycnal. Black and white contours (4, 6, 8, and 10 m) indicate a deepening and shallowing of the mean 1027.25 isopycnal depth, respectively.

circulation (Peru upwelling, central Chile upwelling, PCUC). We chose the single open boundary north of 15°N so that the equatorial dynamics is fully resolved in the parent coarser (1/4°) simulation. Despites the coarser resolution, the ENSO signal is well reproduced in the parent grid and propagates along the coasts of Peru and Chile. In particular, downwelling Kelvin waves modulate the in situ and modeled coastal SSH (strong positive SSH anomaly during 1982–1983 and 1997–1998 El Niño years).

The model results are used to characterize the eddy field of the Southeast Pacific. Both surface and subsurface eddy fields are analyzed. Similar to the modeling study of *Kurian et al*. [2011] on the California Current System, the model results indicate an asymmetry of the surface and subsurface eddy fields. While the number of surface-intensified cyclones is ∼20% higher than surface-intensified anticyclones, we find ∼89% more subsurface anticyclones than subsurface cyclones. Composite maps show that ITEs (subsurface-intensified anticyclone eddies) have a maximum vorticity around 150–200 m depth, which corresponds to the depth of the PCUC. Note that the model PCUC is slightly shallower than in observations probably due to the degree of realism of the ERA_interim wind. Consistent with observed ITEs, model ITEs are associated with a warmer and more saline core. The use of model tracers also confirms the PCUC origin of the ITEs.

The model results are also used to describe the circulation variability from 1979 to 2012. The PCUC transport exhibits a significant intraseasonal, seasonal, and interannual variability. Although the PCUC originates at the low latitudes, the local surface wind stress also modulates the strength of the PCUC. In particular, the PCUC transport is associated with a strong seasonal variability at 36°S–31°S while no significant seasonality is observed at 25°S–20°S. At interannual variability, while the PCUC transport is found to be stronger during strong El Niño years (e.g., 1982–1983, 1997–1998), the number of ITEs decreases. Over the period 1979–2012, both eddy count and volume of ITEs (within 500 km from the coast) shows a significant correlation with the equatorial variability (Niño 3.4 index), associated with variations of the isopycnals depth below the thermocline.

A recent study off central Chile has shown evidence of how the transport of high-nutrient ESSW by subsurface ITEs may influence the productivity offshore [personal communication]. Using satellite chlorophyll, altimetry and oceanic cruises data, the latter study identifies interactions between ITEs formed at the coast between 33°S and 39°S and the Juan Fernandez Archipelago off Chile at ∼33°S. Although the ITEs are associated with a weak surface signature, they highlighted one particular ITE (∼100 km diameter, ∼400 m thick) which interacts with the islands during a period of ∼9 weeks. During this period, they observed a clear increase of surface chlorophyll-a, which corroborates the importance of ITEs in the net transport of coastal

water offshore. A similar model approach (with higher spatial resolution) than the one presented in our study would therefore be a great improvement in the understanding of the ITEs' effects on island/seamount's productivity.

Acknowledgments
Data to support this article are obtained by the modeling experiments explained in the model section. This article greatly benefitted from the insightful comments and criticisms of three anonymous reviewers. We acknowledge the financial support of the National Science Foundation through Grant OCE-0928348, and NASA through Grants NNX08AR40G and NNX12AF67G. The manuscript were partially supported by the FONDECYT Project 1131047 (CONICYT-Chile). Additional support for SH was provided by the Instituto Milenio de Oceanografía (IMO-Chile), funded by the Iniciativa Científica Milenio (ICM-Chile).

References

Aguirre, C., Ó. Pizarro, P. T. Strub, R. Garreaud, and J. A. Barth (2012), Seasonal dynamics of the near-surface alongshore flow off central Chile, *J. Geophys. Res.*, *117*, C01006, doi:10.1029/2011JC007379.

Amante, C., and B. W. Eakins (2009), ETOPO1 1 Arc-Minute Global Relief Model: Procedures, Data Sources and Analysis. NOAA Technical Memorandum NESDIS NGDC-24. National Geophysical Data Center, NOAA, doi:10.7289/V5C8276M.

Beckmann, A., and D. B. Haidvogel (1993), Numerical simulation of flow around a tall isolated seamount. Part I: Problem formulation and model accuracy, *J. Phys. Oceanogr.*, *23*, 1736–1753.

Cambon, G., K. Goubanova, P. Marchesiello, B. Dewitte, S. Illig, and V. Echevin (2013), Assessing the impact of downscaled winds on a regional ocean model simulation of the Humboldt system, *Ocean Modell.*, *65*, 11–24.

Carton, J. A., and B. S. Giese (2008), A reanalysis of ocean climate using simple ocean data assimilation (SODA), *Mon. Weather Rev.*, *136*, 2999–3017.

CERSAT (2002), Mean wind fields (MWF product) user manual volume 1: QuikSCAT, *Rep. C2-MUT-W-04-IF*, Centre ERS d'Archivage et de Traitement - Institut Français de Recherche pour l'Exploitation de la Mer (CERSAT-IFREMER), Brest.

Chaigneau, A., and O. Pizarro (2005), Eddy characteristics in the eastern South Pacific, *J. Geophys. Res.*, *110*, C06005, doi:10.1029/2004JC002815.

Chaigneau, A., M. Le Texier, G. Eldin, C. Grados, and O. Pizarro (2011), Vertical structure of mesoscale eddies in the eastern South Pacific Ocean: A composite analysis from altimetry and Argo profiling floats, *J. Geophys. Res.*, *116*, C11025, doi:10.1029/2011JC007134.

Chelton, D. B., M. G. Schlax, R. M. Samelson, and R. A. de Szoeke (2007), Global observations of large oceanic eddies, *Geophys. Res. Lett.*, *34*, L15606, doi:10.1029/2007GL030812.

Chelton, D. B., M. G. Schlax, and R. M. Samelson (2011), Global observations of nonlinear mesoscale eddies, *Prog. Oceanogr.*, *91*(2), 167–216.

Colas, F., J. C. McWilliams, X. Capet, and J. Kurian (2012), Heat balance and eddies in the Peru-Chile current system, *Clim. Dyn.*, *39*, 509–529, doi:10.1007/s00382-011-1170-6.

Combes, V., and R. P. Matano (2014), A two-way nested simulation of the oceanic circulation in the Southwestern Atlantic, *J. Geophys. Res. Oceans*, *119*, 731–756, doi:10.1002/2013JC009498.

Da Silva, A. M., C. C. Young, and S. Levitus (1994), Atlas of Surface Marine Data 1994, Vol. 1: Algorithms and Procedures. NOAA Atlas NESDIS 6, 83 pp., U.S. Gov. Print. Off., Washington, D. C.

Debreu, L., P. Marchesiello, P. Penven, and G. Cambon (2011), Two-way nesting in split-explicit ocean models: Algorithms, implementation and validation, *Ocean Modell.*, *49–50*, 1–21.

Dee, D. P., et al. (2011), The ERA-Interim reanalysis: Configuration and performance of the data assimilation system, *Q. J. R. Meteorol. Soc.*, *137*, 553–597, doi:10.1002/qj.828.

Fairall, C. W., E. F. Bradley, D. P. Rogers, J. B. Edson, and G. S. Young (1996), Bulk parameterization of air-sea fluxes for tropical ocean-global atmosphere Coupled-Ocean Atmosphere Response Experiment, *J. Geophys. Res.*, *101*, 3747–3764.

Gunther, E. R. (1936), A report on oceanographical investigation in Peru Coastal Current, *Discovery Rep.*, *13*, 107–276.

Hormazabal, S., V. Combes, C. E. Morales, M. A. Correa-Ramirez, E. Di Lorenzo, and S. Nuñez (2013), Intrathermocline eddies in the coastal transition zone off central Chile (31–41°S), *J. Geophys. Res. Oceans*, *118*, 4811–4821, doi:10.1002/jgrc.20337.

Huyer, A., M. Knoll, T. Paluszkiewicz, and R. L. Smith (1991), The Peru undercurrent: A study in variability, *Deep Sea Res., Part A*, *38*, suppl. 1, 247–279.

Illig, S., B. Dewitte, K. Goubanova, G. Cambon, J. Boucharel, F. Monetti, C. Romero, S. Purca, and R. Flores (2014), Forcing mechanisms of intraseasonal SST variability off central Peru in 2000– 2008, *J. Geophys. Res. Oceans*, *119*, 3548–3573, doi:10.1002/2013JC009779.

Isern-Fontanet, J., E. Garcia-Ladona, and J. Font (2006), Vortices of the Mediterranean sea: An altimetric perspective, *J. Phys. Oceanogr.*, *36*, 87–103.

Johnson, G. C., and K. E. McTaggart (2009), Equatorial Pacific 13°C water eddies in the eastern subtropical south Pacific Ocean, *J. Phys. Oceanogr.*, *40*, 226–236.

Kanamitsu, M., W. Ebisuzaki, J. Woollen, S.-K. Yang, J. J. Hnilo, M. Fiorino, and G. L. Potter (2002), NCEP–DOE AMIP-II Reanalysis (R-2), *Bull. Amer. Meteor. Soc.*, *83*, 1631–1643, doi:10.1175/BAMS-83-11-1631.

Kurian, J., F. Colas, X. Capet, J. C. McWilliams, and D. B. Chelton (2011), Eddy properties in the California current system, *J. Geophys. Res.*, *116*, C08027, doi:10.1029/2010JC006895.

Large, W., J. McWilliams, and S. Doney (1994), Oceanic vertical mixing—A review and a model with a nonlocal boundary-layer parameterization, *Rev. Geophys.*, *32*, 363–403.

Marchesiello, P., J. C. McWilliams, and A. Shchepetkin (2001), Open boundary conditions for long-term integration of regional oceanic models, *Ocean Modell.*, *3*, 1–20.

Marchesiello, P., L. Debreu, and X. Couvelard (2009), Spurious diapycnal mixing in terrain-following coordinate models: The problem and a solution, *Ocean Modell.*, *26*, 156–169.

Masumoto, Y., et al. (2004), A fifty year eddy-resolving simulation of the World Ocean—Preliminary outcomes of OFES (OGCM for the Earth Simulator), *J. Earth Simulator*, *1*, 31–52.

Montes, I., W. Schneider, F. Colas, B. Blanke, and V. Echevin (2011), Subsurface connections in the eastern tropical Pacific during La Niña 1999–2001 and El Niño 2002–2003, *J. Geophys. Res.*, *116*, C12022, doi:10.1029/2011JC007624.

Morales, C. E., S. Hormazabal, M. Correa-Ramirez, O. Pizarro, N. Silva, C. Fernandez, V. Anabalon, and M. L. Torreblanca (2012), Mesoscale variability and nutrient–phytoplankton distributions off central-southern Chile during the upwelling season: The influence of mesoscale eddies, *Prog. Oceanogr.*, *104*, 17–29, doi:10.1016/j.pocean.2012.04.015.

Pizarro, O., G. Shaffer, B. Dewitte, and M. Ramos (2002), Dynamics of seasonal and interannual variability of the Peru-Chile Undercurrent, *Geophys. Res. Lett.*, *29*(12), 1581, doi:10.1029/2002GL014790.

Ramos, M., O. Pizarro, L. Bravo, and B. Dewitte (2006), Seasonal variability of the permanent thermocline off northern Chile, *Geophys. Res. Lett.*, *33*, L09608, doi:10.1029/2006GL025882.

Röske, F. (2006), A global heat and freshwater forcing dataset for ocean models, *Ocean Modell.*, *11*, 235–297.

Sasaki, H., Y. Sasai, S. Kawahara, M. Furuichi, F. Araki, A. Ishida, Y. Yamanaka, Y. Masumoto, and H. Sakuma (2004), A series of eddy resolving ocean simulations in the world ocean: OFES (OGCM for the Earth Simulator) project, in Bridges Across the Oceans: Techno-Ocean '04, vol. 3, pp. 1535–1541, Mar. Technol. Soc., Columbia, Md.

Sasaki, H., M. Nonaka, Y. Masumoto, Y. Sasai, H. Uehara, and H. Sakuma (2008), An eddy-resolving hindcast simulation of the quasi-global ocean from 1950 to 2003 on the Earth Simulator, in *High Resolution Numerical Modelling of the Atmosphere and Ocean*, edited by K. Hamilton and W. Ohfuchi, pp. 157–185, Springer, N. Y.

Shaffer, G., S. Hormazabal, O. Pizarro, and S. Salinas (1999), Seasonal and interannual variability of winds, current and temperature near the coast of Chile, *J. Geophys. Res.*, *104*, 29,951–29,961.

Shchepetkin, A., and J. C. McWilliams (2005), The regional oceanic modeling system (ROMS): A split explicit, free-surface, topography-following-coordinate oceanic model, *Ocean Modell.*, *9*, 347–404.

Silva, N., N. Rojas, and A. Fedele (2009), Water masses in the Humboldt current system: Properties, distribution, and the nitrate deficit as a chemical water mass tracer for Equatorial subsurface water off Chile, *Deep Sea Res., Part II*, *56*(16), 1004–1020, doi:10.1016/j.dsr2.2008.12.013.

Silva N. S., and S. Neshyba (1979), On the southernmost extension of the Peru-Chile Undercurrent, *Deep Sea Res., Part A*, *26*, 1387–1393.

Strub, P. T., J. M. Mesias, V. Montecino, J. Rutllant, and S. Salinas (1998), Coastal ocean circulation off western South America, in *The Sea*, vol. 11, edited by A. R. Robinson and K. H. Brink, pp. 273–313, John Wiley, N. Y.

Wooster, W. S., and M. Gilmartin (1961), The Peru-Chile undercurrent, *J. Mar. Res.*, *19*(3), 97–122.